SARM1 is responsible for calpain-dependent dendrite degeneration in mouse hippocampal neurons

Received for publication, July 21, 2023, and in revised form, December 10, 2023 Published, Papers in Press, January 8, 2024,
https://doi.org/10.1016/j.jbc.2024.105630

Takashi Miyamoto, Chaeyoung Kim, Johann Chow, Jason C. Dugas, Jack DeGroot, Alex L. Bagdasarian, Arun P. Thottumkara, Martin Larhammar, Meredith EK. Calvert, Brian M. Fox, Joseph W. Lewcock*, and Lesley A. Kane*

From Denali Therapeutics Inc, South San Francisco, California, USA

Reviewed by members of the JBC Editorial Board. Edited by Elizabeth J. Coulson

Sterile alpha and toll/interleukin receptor motif-containing 1 (SARM1) is a critical regulator of axon degeneration that acts through hydrolysis of NAD^+ following injury. Recent work has defined the mechanisms underlying SARM1's catalytic activity and advanced our understanding of SARM1 function in axons, yet the role of SARM1 signaling in other compartments of neurons is still not well understood. Here, we show in cultured hippocampal neurons that endogenous SARM1 is present in axons, dendrites, and cell bodies and that direct activation of SARM1 by the neurotoxin Vacor causes not just axon degeneration, but degeneration of all neuronal compartments. In contrast to the axon degeneration pathway defined in dorsal root ganglia, SARM1-dependent hippocampal axon degeneration *in vitro* is not sensitive to inhibition of calpain proteases. Dendrite degeneration downstream of SARM1 in hippocampal neurons is dependent on calpain 2, a calpain protease isotype enriched in dendrites in this cell type. In summary, these data indicate SARM1 plays a critical role in neurodegeneration outside of axons and elucidates divergent pathways leading to degeneration in hippocampal axons and dendrites.

Distal axon degeneration following injury follows a pattern that was originally termed Wallerian degeneration (1, 2). It was initially believed that this degeneration was passive, but this changed after the identification of the Wallerian degeneration slow (WLDS) mouse strain that displayed significantly delayed axon degeneration following injury (3). The WLDS mutation was subsequently shown to be a fusion of ubiquitination factor E4B (UBE4B) and nicotinamide mononucleotide adenylyltransferase 1 (NMNAT1) (4). This fusion protein persists in damaged axons and has been shown to be protective in injury models of cultured dorsal root ganglion (DRG) or superior cervical ganglion (SCG) neurons and mouse sciatic nerves (5–7). NMNAT1 is an enzyme that converts nicotinamide mononucleotide (NMN) into NAD^+ that is usually localized to the nucleus, but the UBE4B-NMNAT1 fusion protein is diffusely localized and stabilized. This results in active enzyme that persists in damaged axons and preserves NAD^+ levels following injury (8). Further studies in SCG neurons revealed that the endogenous protein responsible for maintaining NAD^+ levels in axons is another NMNAT isoform, NMNAT2, which is rapidly lost upon axon injury (9).

A subsequent forward genetic screen in *Drosophila melanogaster* led to the discovery of the first mutations that slowed Wallerian degeneration (10). This study identified sterile alpha and Armadillo motif (*dSarm*) and its mouse ortholog sterile alpha and toll/interleukin receptor (TIR) motif-containing protein 1 (*Sarm1*) as a novel regulator of axon degeneration. Deletion of *dSarm*/*Sarm1* in flies, primary mouse cortical, SCG, DRG neurons, and mouse sciatic nerve delayed axon degeneration following injury. The mechanism by which SARM1 regulates axon degeneration became clearer upon the discovery of a noncanonical NAD^+ hydrolase function of its TIR domain (11). Isolated recombinant or cellular SARM1 hydrolyzes NAD^+ into nicotinamide, adenosine diphosphate ribose (ADPR), and cyclic-ADPR (cADPR) (11–14). SARM1's intrinsic NAD^+ hydrolase activity, along with the known roles of WLDS and NMNAT2 in NAD^+ metabolism, solidified SARM1-dependent NAD^+ hydrolysis as a critical step in the axon degeneration pathway (1, 2). Taken together, these data have led to a model in which degradation of NMNAT2 lowers NAD^+ and increases NMN following axonal injury (15–17). NMN then directly activates SARM1, leading to a further reduction of NAD^+ (2, 14, 18–25). Structural investigations confirmed an allosteric binding pocket in SARM1, normally occupied by NAD^+ but replaced by NMN to induce hydrolase activity (2, 14, 18, 21, 22, 24, 26, 27). It has been hypothesized that other prodegenerative stimuli may similarly alter the NAD^+/NMN ratio to favor activation of SARM1 (15, 18, 24, 27).

Research on SARM1 has focused on its role in axon degeneration following axotomy or treatment with chemotherapeutics (1, 2, 28) and therefore our understanding of mammalian SARM1 function comes predominantly from studies in DRG/SCG neurons as a model system (1, 28, 29). This specialized population of sensory neurons have a single axon that bifurcates into two branches, which has limited our

* For correspondence: Joseph W. Lewcock, lewcock@dnli.com; Lesley A. Kane, kane@dnli.com.
Present addresses for: Jack DeGroot, Intellia Therapeutics, Inc., 40 Erie St, Cambridge, Massachusetts, 02139, USA; Arun P. Thottumkara, Odyssey Therapeutics, 4242 Campus Point Ct, San Diego, California, 92121, USA; Martin Larhammar, BioArctic, Warfvinges väg 35, 112 51, Stockholm, Sweden.

understanding of SARM1 function in other neuronal compartments. Wallerian degeneration of dendrites has been reported in *Drosophila* (30, 31), but there is limited evidence for the pathway in dendrites of mammalian neurons. In this study, we outline the degenerative properties of SARM1 in mouse primary hippocampal neurons that have complex morphology and processes. Using these neurons we show the presence of SARM1 protein and activity outside of axons and define a role for SARM1 in dendrite degeneration through activation of calpain proteases.

Results

SARM1 is present and functional in all neuronal compartments

To better define the role of SARM1 in central nervous system (CNS) neurons, we began by determining the SARM1 localization in cultured primary hippocampal neurons. Immunostaining for endogenous SARM1 in *wildtype* neurons revealed punctate, but specific signal throughout the cells (Fig. 1*A* – Top row) which was absent in neurons from *Sarm1*-knockout (*Sarm1KO*) mice (Fig. 1*A* – Middle row). We next examined a 1:1 ratio mixed culture of *wildtype* and *Sarm1KO* neurons which allowed us to both confirm the specificity of the SARM1 antibody by observing cells with (Fig. 1*A* – Bottom row, arrow) and without (Fig. 1*A* – Bottom row, arrowhead) signal and to better observe morphological details of each SARM1-positive neuron. Using super-resolution microscopy, we then investigated the presence of SARM1 in neuronal compartments marked by axonal (SMI312) and dendrite (MAP2) markers and found that endogenous SARM1 is present in axons, dendrites, and cell bodies (Fig. 1*B* – zoomed in image and line graph).

We next sought to test SARM1 activity in each neuronal compartment following direct activation by CZ-48 or Vacor, two cell permeable compounds that have been reported to mimic NMN, an endogenous SARM1 activator (20, 23, 32). CZ-48 is an inhibitor of CD38, another NADase that was unexpectedly found to activate SARM1 (20), and Vacor was used as a rodenticide and its accidental ingestion can cause peripheral and central neuropathy and/or diabetes mellitus in humans (33, 34). While CZ-48 is an NMN analog, Vacor requires processing by nicotinamide phosphoribosyltransferase to produce the NMN analog Vacor mononucleotide, which directly activates SARM1 (20, 23, 32). To directly observe SARM1 activity, we employed PC6/PAD6, a live-cell SARM1 activity probe. PAD6 is formed as an adduct of PC6 and ADPR generated by SARM1 upon NAD^+ hydrolysis that causes a red shift in fluorescence and allows for the direct measurement of SARM1 activity in live cells (35). Neurons were preloaded with PC6, treated with a wide concentration range of SARM1 activators, and then imaged for PAD6 signal at two time points – 1, and 2 h after the addition of SARM1 agonists. Following SARM1 activation with CZ-48 (Fig. 1, *C* and *D*) or Vacor (Fig. 1, *E* and *F*), *wildtype*, but not *Sarm1KO*, neurons displayed diffuse fluorescent signal throughout cell bodies and neurites, indicating the signal was induced by SARM1-dependent PAD6 formation across all the neuronal compartments. The PAD6 signal was also ablated by cotreatment with a SARM1 inhibitor (36) in *wildtype* neurons (Fig. S1, *A* and *B*). PC6-loaded *wildtype* and *Sarm1KO* neurons both displayed some punctate background signal in the control conditions that overlapped with lysosomes (Fig. S1*C*), suggesting protonation of PC6 in acidic lysosomes that was independent of SARM1 activity. However, this background punctate signal could be readily separated from the widespread PAD6 signal observed throughout neurons by measuring the increase in total PAD6-positive area (Fig. 1, *C* and *E*). Following activation of SARM1 in hippocampal neurons by either CZ-48 or Vacor, total cellular NAD(H) was lost in a SARM1-dependent manner (Fig. 1*G*). This ubiquitous PAD6 signal and complete loss of cellular NAD(H) indicates that SARM1 is functional and can be activated both inside and outside of axons in hippocampal neurons.

Direct SARM1 activation results in degeneration of multiple neuronal compartments

To gain a better understanding of the consequences of SARM1 activation in distinct subcellular compartments, we directly activated SARM1 using a wide concentration range of CZ-48 or Vacor and then assessed the extent of degeneration at a single time point (16 h) by immunostaining for markers of axons (SMI312) and dendrites (MAP2), as well as quantifying nuclear condensation (4′,6-diamidino-2-phenylindole [DAPI]). Both compounds resulted in a dose-dependent degeneration of both axons and dendrites in *wildtype*, but not *Sarm1KO*, neurons (Fig. 2, *A*–*D*). Neurons treated with very high (≥50 μM) concentrations of Vacor also showed SARM1-independent degeneration, presumably a result of off-target toxicity (Fig. 2*D*). Degeneration of neuronal processes following CZ-48/Vacor treatment was similarly attenuated by pharmacological inhibition of SARM1 activity (Fig. S2*A*). Vacor and CZ-48 also caused a SARM1-dependent increase in condensed nuclei, suggesting that in this setting SARM1 activation can be sufficient to drive cell death in addition to neurite degeneration (Fig. 2, *A*–*D*).

All neuronal compartments (axons, dendrites, and cell bodies) had the same relative sensitivity to CZ-48 and Vacor, indicating that no one compartment is more sensitive to SARM1 activation. Vacor was a more potent activator with maximal degeneration occurring at 6.25 μM, while CZ-48 did not reach maximal levels even at 1 mM (Fig. 2, *B* and *D*). However, simultaneous addition of the nicotinamide phosphoribosyltransferase inhibitor FK866 potentiated the degeneration of all neuronal compartments observed following CZ-48 treatment (Fig. S2*B*), presumably a result of more robust lowering of NAD^+ levels (14, 18, 22). The addition of FK866 sensitized axons, dendrites, and cell bodies to CZ-48 to the same degree with degeneration evident at concentrations ≥0.25 mM and maximal degeneration occurring at 0.5 mM (Fig. S2*B*).

SARM1-mediated dendrite degeneration is calpain-dependent

Calcium (Ca^{2+}) influx and activity of calpains (Ca^{2+}-dependent proteases), are known contributors to axon

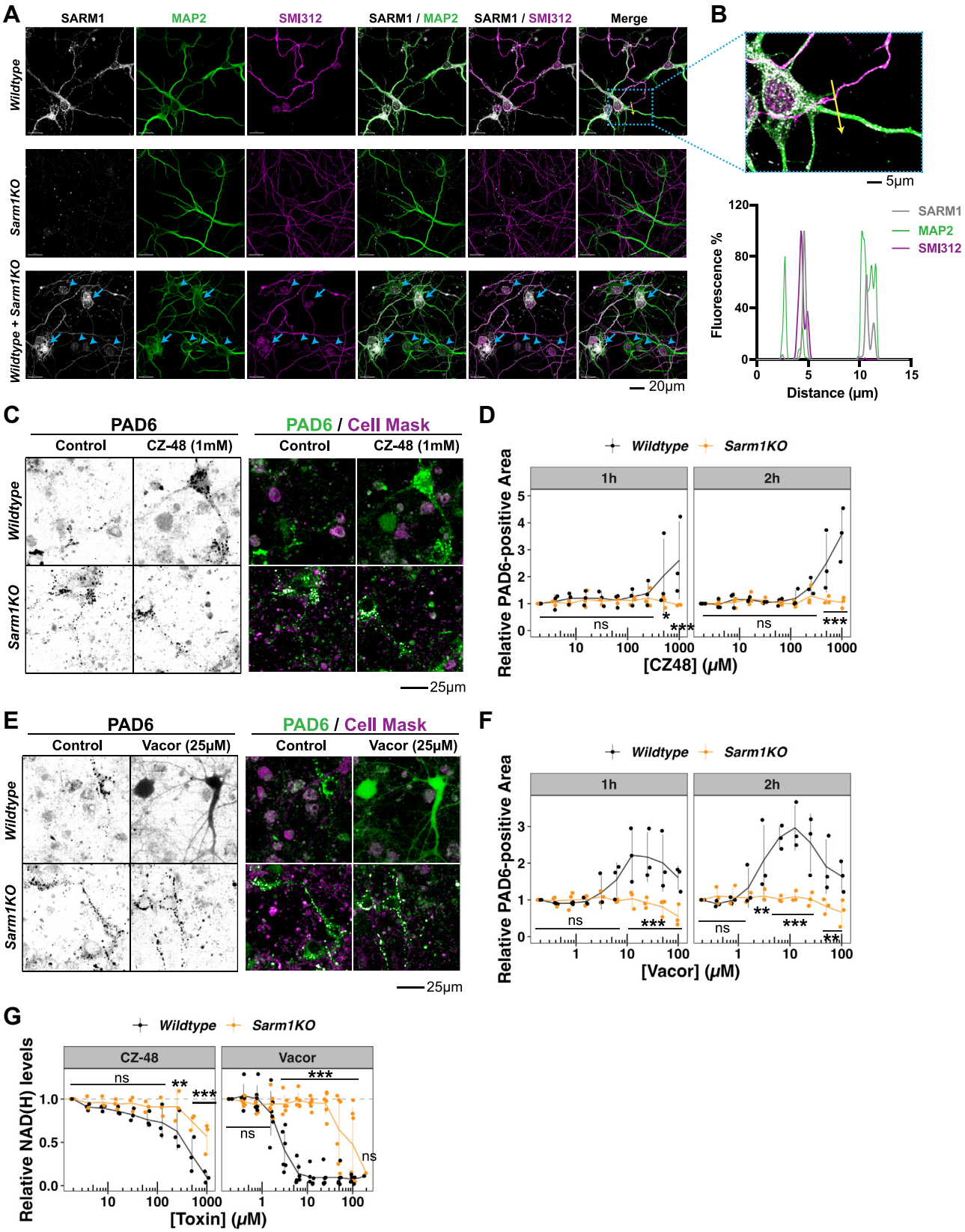

Figure 1. SARM1 is present and can be activated in all neuronal compartments. *A*, representative images of the primary cultured hippocampal neurons ("neurons") from *wildtype* and *Sarm1KO* mice, and the mixed culture of the two genotypes that were immunostained for endogenous SARM1 (*grayscale*), axonal (SMI312, *magenta*), and dendritic (MAP2, *green*) marker proteins. In the mixed neuron culture, *blue arrows* and *arrowheads* point at *wildtype* and *Sarm1KO* neurons, respectively, that were identified based on the SARM1 immunostaining. *B*, a zoomed-in image of the *wildtype* neurons in (*A*)—the area defined by the *blue dashed box* in the merged image of *wildtype* neurons (*top*), and the line graph that indicates the relative intensity of SARM1, MAP2, and SMI312 immunostaining along the *yellow arrow* indicated in the zoomed-in image (*bottom*). *C–F*, SARM1 activity in *wildtype* and *Sarm1KO* neurons treated

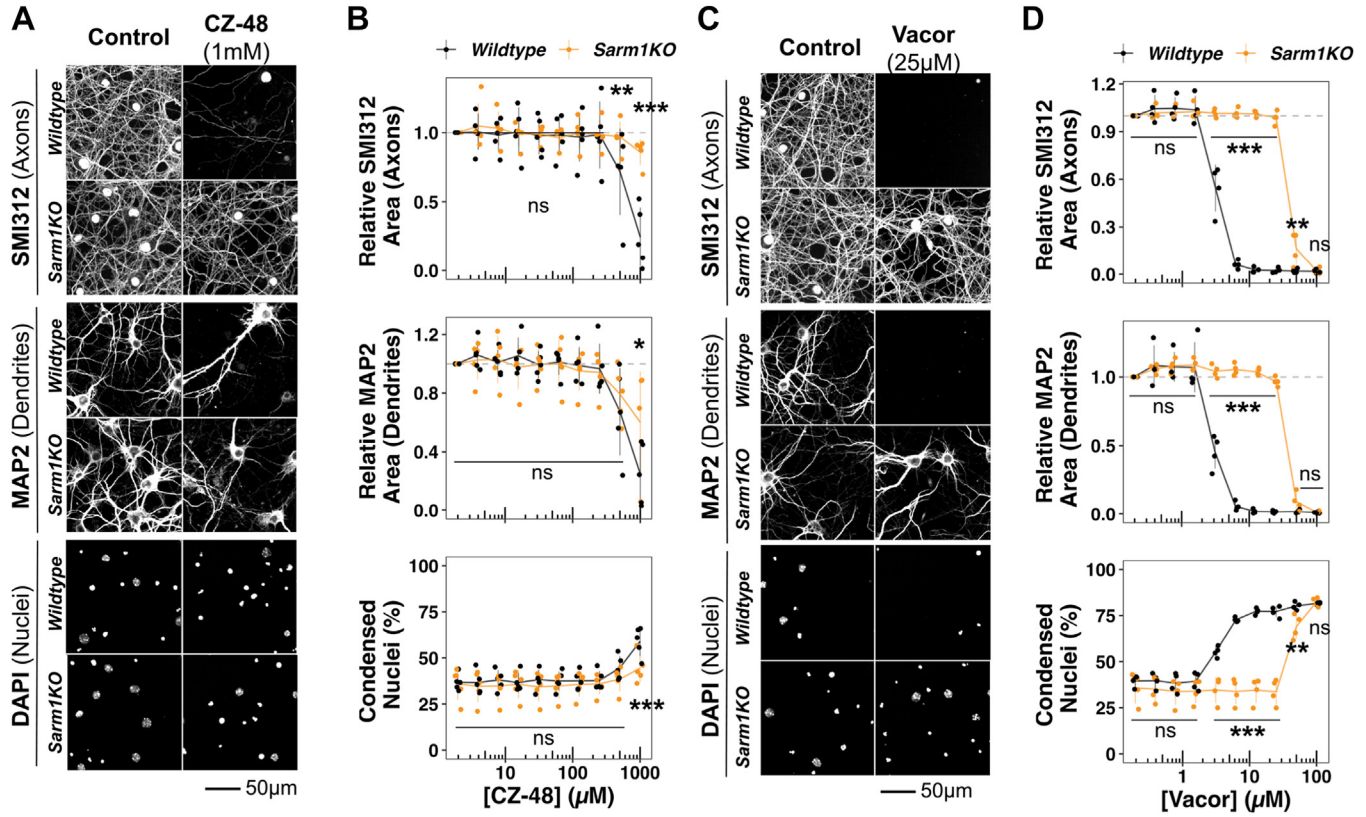

Figure 2. SARM1 activation degenerates all neuronal compartments. Representative images and relative levels of immunostained axons and dendrites, and proportion of condensed nuclei in *wildtype* and *Sarm1KO* neurons that were treated with increasing concentrations of (*A* and *B*) CZ-48 or (*C* and *D*) Vacor for 16 h. All representative images from the same group were taken in the same field of the same neuronal culture. Statistical significance of differences among groups was determined by two-way ANOVA using genotype and toxin doses as two independent variables. When the effect of genotype was significant ($p < 0.05$), Tukey's post hoc test was performed and p values that are less than 0.05 for comparisons between the two genotypes at the specific toxin doses are shown. Number of biologically independent experiments (n) are (*B*) 5, and (*D*) 4. Data are represented as the mean ± standard deviation by *vertical lines* with individual data points shown by *small circles*. *$p < 0.05$, **$p < 0.01$, ***$p < 0.001$, ns $p \geq 0.05$. SARM1, sterile alpha and toll/interleukin receptor motif-containing 1.

degeneration following injury or SARM1 activation in DRG/SCG neurons (37–42). Based on these findings, we investigated the involvement of calpains in SARM1-dependent degeneration of hippocampal neuron compartments by cotreating neurons with Vacor and several commonly used calpain inhibitors (Fig. S3, *A* and *B*). Calpain inhibitor III, calpeptin, and PD150606 are relatively selective to calpain1 and calpain2, compared to (2S,3S)-*trans*-Epoxysuccinyl-L-leucylamido-3-methylbutane ethyl ester and leupeptin that also inhibit other types of proteases (43–45). Surprisingly, none of the calpain inhibitors prevented Vacor-dependent degeneration of SMI312-positive axons even when used at high concentrations (30 μM) (Figs. 3, *A* and *B* and S3, *A* and *B*). In contrast, calpain inhibitor III and calpeptin robustly prevented Vacor-dependent degeneration of MAP2-positive dendrites (Figs. 3, *A* and *B* and S3, *A* and *B*). Calpain inhibition also protected dendrites against direct activation of SARM1 by CZ-48/FK866, further supporting the notion that calpains act downstream of SARM1 (Fig. S3, *C* and *D*).

To determine whether calpain activation and dendrite degeneration is dependent on caspases as was observed in DRG axons following lesion or trophic factor withdrawal (46, 47), we next tested the pan-caspase inhibitor Q-VD-OPh. Caspase inhibition had no effect on SARM1-dependent dendrite degeneration, demonstrating specificity of calpain proteases in this process and suggesting distinct upstream signals lead to calpain activation in this context (Fig. S4). Interestingly, Q-VD-OPh also failed to protect axons of hippocampal neurons from SARM1-dependent degeneration (Fig. S4). To confirm that the loss of MAP2 immunostaining represents degeneration of dendrites, we immunostained drebrin, another dendritic marker protein that is enriched in dendritic spines (48) as opposed to MAP2 that is enriched in dendritic shafts (Fig. S5*A*). The correlation of MAP2 and

with CZ-48 (*C* and *D*) or Vacor (*E* and *F*) shown by both representative images at 1 h (*C* and *E*, *grayscale* (*left*) and overlaid with CellMask staining (*right*)) and quantification of PAD6-positive area for 1 or 2 h (*D* and *F*). *G*, cellular NAD(H) levels of *wildtype* and *Sarm1KO* neurons that were treated with increasing concentrations of CZ-48 or Vacor for 16 h. Statistical significance of differences among groups was determined by two-way ANOVA using genotype and toxin doses as two independent variables. When the effect of genotype was significant ($p < 0.05$), Tukey's post hoc test was performed and p values that are less than 0.05 for comparisons between the two genotypes at the specific toxin doses are shown. Number of biologically independent experiments (n) are (*D* and *F*) three and (*G*) three (CZ-48) and six (Vacor). Data are represented as the mean ± standard deviation by *vertical lines* with individual data points shown by *small circles*. *$p < 0.05$, **$p < 0.01$, ***$p < 0.001$, ns $p \geq 0.05$. SARM1, sterile alpha and toll/interleukin receptor motif-containing 1.

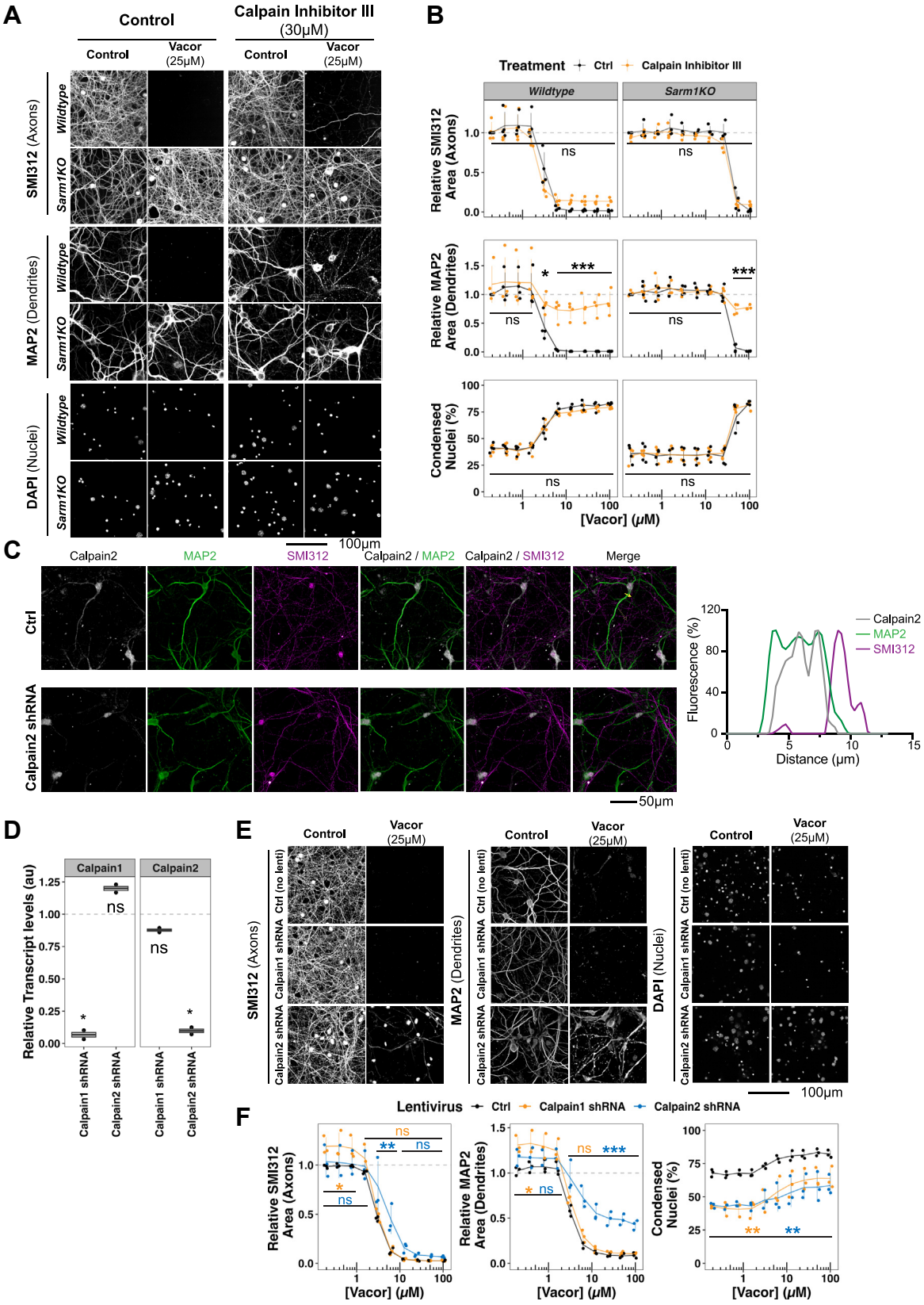

Figure 3. SARM1-induced dendrite degeneration depends on calpains. *A*, representative images and (*B*) relative levels of immunostained axons and dendrites, and proportion of condensed nuclei in *wildtype* and *Sarm1KO* neurons that were treated with various concentrations of Vacor for 16 h. Some neurons were cotreated with calpain inhibitor III (30 μM). *C*, representative immunofluorescent images and a line graph of primary mouse hippocampal neurons from *wildtype* mice. Neurons were immunostained for calpain2 along with axonal (SMI312) and dendritic (MAP2) marker proteins. To validate the specificity of the calpain2 antibody, neurons that were transduced with lentivirus encoding shRNA against calpain2 were also immunostained. The line graph on the *right* indicates the relative intensity of the immunostaining along the *yellow arrow* indicated in the merged images. *D*, calpain1 and calpain2

drebrin immunostaining indicates SARM1- and calpain-dependent dendrite degeneration (Fig. S5).

To confirm a role for calpains in this process and determine the specific calpain isoform that is required for SARM1-dependent dendrite degeneration, we more closely investigated calpain1 and 2, two major calpain isotypes found in neurons (49). We first examined the subcellular localization of calpain1 and calpain2 by immunostaining. Although both isotypes were present in our hippocampal neuron cultures, calpain2 appeared to be enriched in dendrites compared to axons (Figs. 3*C* and S6). We next used shRNA to specifically knock down either calpain1 or calpain2. Only calpain2 knockdown specifically protected against Vacor-induced dendrite degeneration (Fig. 3, *C–F*), indicating that it is the primary calpain isoform responsible for SARM1-dependent degeneration in hippocampal neurons. The dendrite enriched expression of calpain2 suggests that the differential impact of calpain inhibition or knock down in dendrites as compared to axons may result from the localization of calpain2 protein.

To confirm that calpain activation occurs downstream of SARM1, we delayed the addition of either a SARM1 or calpain inhibitor until after activating SARM1 (Fig. 4*A* for experimental design). Based on the robust protection of dendrites (Figs. 3 and S3) and known selectivity and potency, calpain inhibitor III was chosen for subsequent experiments. Delayed addition of an SARM1 inhibitor protected dendrites when added within two hours of Vacor treatment (Fig. 4, *B* and *C*, orange shading), whereas calpain inhibitor III protected dendrites if added up to three hours after Vacor treatment (Fig. 4, *B* and *C*, blue shading). The window of 1 h where calpain inhibition was still protective beyond SARM1 inhibition suggests that calpains are activated downstream of SARM1 and, once active, are not reversable by SARM1 inhibition. Examination of SARM1 activity following treatment with a calpain inhibitor provided additional evidence that SARM1 acts upstream of calpain activation, as PAD6 fluorescence following cotreatment of hippocampal neurons with CZ-48 or Vacor and calpain inhibitor III was not significantly different than treatment with SARM1 activators alone (Fig. 4, *D* and *E*).

Multiple waves of calcium influx have been described in axon lesion studies, a first transient wave that occurs rapidly after injury and a second prolonged one that occurs hours after injury and is immediately followed by axon fragmentation (39, 40). Given the requirement for calcium influx in calpain activation, we hypothesized that SARM1 activity contributes to calcium influx in hippocampal neurons. To test this, we monitored intracellular calcium levels by Fluo4 intensity following Vacor treatment. Vacor had no effect on calcium influx at early time points (≤1 h) but resulted in a significant increase in Fluo4 signal in *wildtype* neurons at later time points (≥2 h) (Figs. 5, *A* and *B* and S7*A* for all time points and treatments). Interestingly, Fluo4 signal did not increase at any time point in either *Sarm1KO* neurons or *wildtype* neurons treated with either EGTA or a SARM1 inhibitor, indicating that it is both extracellular calcium and SARM1 activity-dependent (Figs. 5, *A* and *B* and S7*A* for all time points and treatments). We next sought to determine the calcium channels acting downstream of SARM1 activation. Among several voltage-gated calcium channels (Cav) blockers, cilnidipine prevented a large portion of calcium influx induced by Vacor (Fig. 5, *C* and *D*), whereas the other blockers, including nifedipine, had no effect on calcium influx (Fig. S7*B*). This suggests that Cav2.2 channels conduct calcium influx induced by SARM1 activity in neurons as cilnidipine and nifedipine block Cav1/2.2 and Cav1 channels respectively (50).

Calpains are downstream executors of SARM1 degeneration in dendrites, but not axons

Several axon-specific calpain substrates have been identified including neurofilament light (Nf-L) and stathmin 2 in axon degeneration in DRG neurons (37, 41, 51, 52). Consistent with previous reports, we observed Nf-L cleavage and loss of stathmin 2 upon SARM1 activation by Vacor treatment in cultured mouse DRG neurons, which was prevented following addition of calpain inhibitor III (Fig. 6, *A* and *B*). EGTA also prevented SARM1-dependent cleavage of Nf-L but depleted stathmin 2 independently of SARM1 (Fig. 6, *A* and *B*), which could be caused by altered microtubule dynamics that rapidly depleted stathmin 2 (52). Although drebrin is enriched in dendrites of hippocampal neurons (Fig. S5), drebrin was expressed also in DRG neurons that do not have dendrites and depleted in SARM1-and calpain-dependent manner, showing the same profile as full-length Nf-L and stathmin 2 (Fig. 6, *A* and *B*).

We next tested whether similar processing of axonal proteins - Nf-L and stathmin 2—occurred in hippocampal neurons. Surprisingly, despite robust axon degeneration following Vacor treatment in hippocampal neurons (Fig. 2), no calpain-dependent processing of Nf-L nor depletion of stathmin 2 occurred (Fig. 6, *C* and *D*). Calpain inhibitor III moderately increased stathmin 2 levels independently of SARM1 activation, suggesting constant calpain-mediated stathmin 2 proteolysis occurs in these neurons (Fig. 6, *C* and *D*). EGTA slightly depleted stathmin 2 independently of SARM1 activation,

transcript levels in neurons that were transduced with lentivirus encoding shRNA against calpain1 and calpain2. The transcript levels were normalized to the neurons that were not transduced with lentivirus in each biological replicate (the levels of control neurons = 1). *E*, representative images and (*F*) relative levels of immunostained axons and dendrites, and proportion of condensed nuclei in *wildtype* neurons that were treated with various concentrations of Vacor for 16 h. Neurons were treated with DMEM (Ctrl) or transduced with lentivirus encoding shRNA against calpain1 or calpain2. In (*B* and *F*), statistical significance of effects by pharmacological treatment or lentiviral transduction was determined by two-way ANOVA using pharmacological treatment or lentiviral transduction, and Vacor doses as two independent variables. When the effect of the inhibitor treatment or lentiviral transduction was significant ($p < 0.05$), Tukey's post hoc test was performed and p values that are less than 0.05 for the effect of inhibitor treatment or lentiviral transduction compared to the control group at the specific toxin doses are shown in figure panels. Data are represented as the mean ± standard deviation by *vertical lines* with individual data points shown by *small circles*. In (*D*), Statistical significance was determined by one sample *t* test using the theoretical mean of 1. Data are represented by *boxplots* with individual points. Number of biologically independent experiments (n) are (*B*) 4, (*D*) 2, and (*F*) 3. *$p < 0.05$, **$p < 0.01$, ***$p < 0.001$, ns $p \geq 0.05$. DMEM, Dulbecco's modified Eagle's medium; SARM1, sterile alpha and toll/interleukin receptor motif-containing 1.

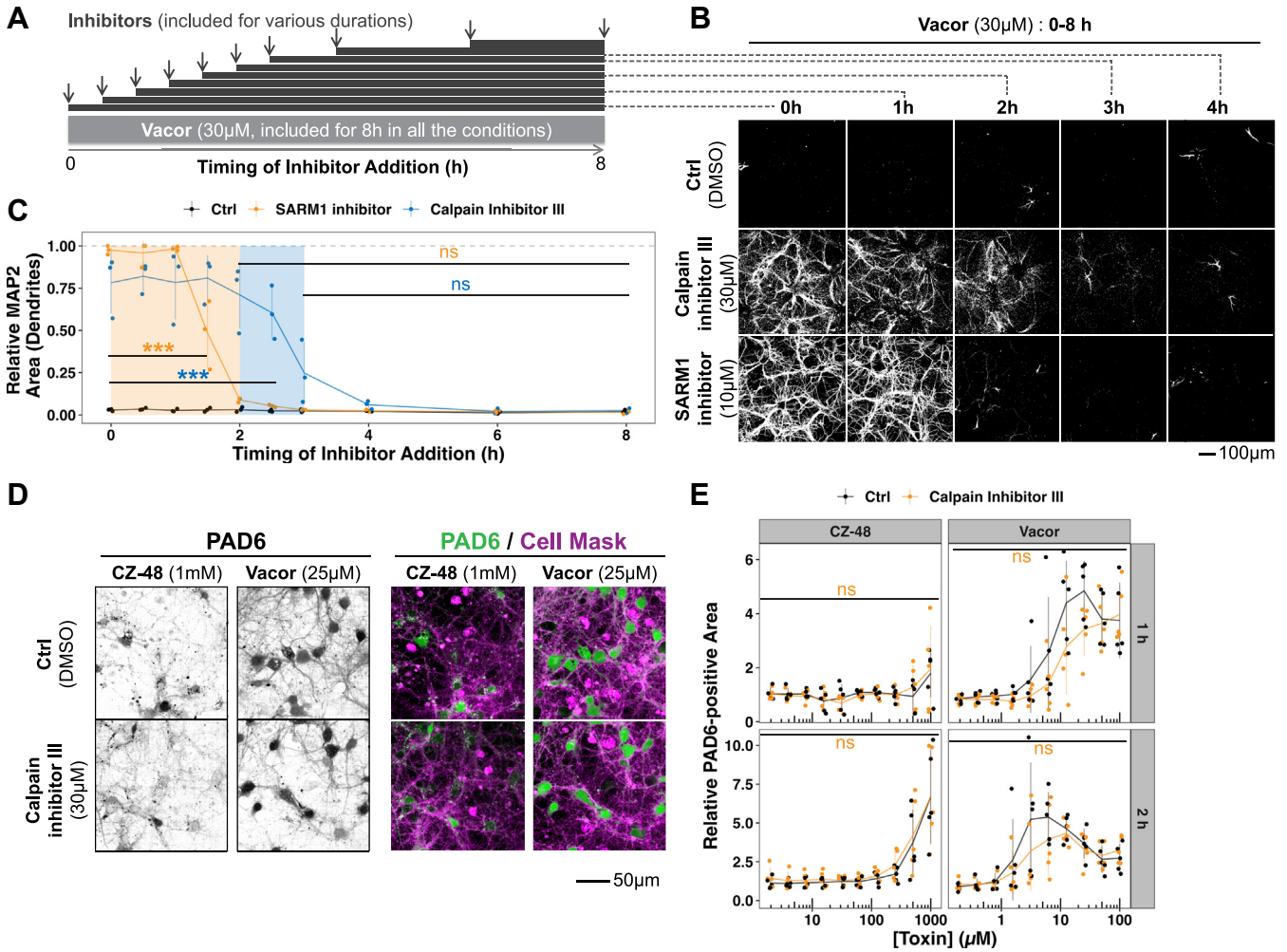

Figure 4. Calpain activation is downstream of SARM1. *A*, schematic diagram of experiment in which inhibitors were applied at multiple time points after beginning Vacor treatment. *B*, representative images and (*C*) relative levels of immunostained dendrites in *wildtype* neurons that were treated with Vacor for 8 h with either calpain inhibitor III or SARM1 inhibitor added at increasing durations after Vacor treatment as indicated in the panel (*A*). *D*, representative images at 1 h and (*E*) relative PAD6 fluorescence levels of PC6-loaded neurons that were treated with increasing concentrations of CZ-48 or Vacor for one or 2 h with or without calpain inhibitor III (30 μM). Statistical significance of effects by inhibitors was determined by two-way ANOVA using (*C*) inhibitor treatment and the timing of inhibitor addition, or (*E*) calpain inhibitor III treatment and Vacor doses as two independent variables. When the effect of the timing of inhibitor addition or inhibitor treatment was significant ($p < 0.05$), Tukey's post hoc test was performed and p values that are less than 0.05 for the effect of inhibitor treatment at the specific toxin doses are shown in a color-matched manner in figure panels. Number of biologically independent experiments (n) are (*C*) four or (*E*) 5. Data are represented as the mean ± standard deviation by *vertical lines* with individual data points shown by *small circles*. $^{*}p < 0.05$, $^{**}p < 0.01$, $^{***}p < 0.001$, ns $p \geq 0.05$. SARM1, sterile alpha and toll/interleukin receptor motif-containing 1.

similarly to DRG neurons. Robust and specific expression of Nf-L in axons and axonal enrichment of stathmin 2 were confirmed by immunostaining in these neurons, indicating that this discrepancy was not a result of changes in subcellular localization (Fig. S8, *A* and *B*). This lack of Nf-L processing or stathmin 2 depletion by calpains is consistent with the lack of axonal protection afforded by calpain inhibition in this paradigm.

As dendrites were specifically protected by calpain inhibition following Vacor we moved on to measure the cleavage of αII-spectrin, α-internexin, and drebrin, three calpain substrates that are present primarily in dendrites of hippocampal neurons (48, 53, 54) (Fig. S8, *C*–*E*). All three proteins were substantially degraded by treatment with 30 μM Vacor for 3 h (Fig. 6, *E* and *F*). This processing was completely blocked by cotreatment with a SARM1 or calpain inhibitor, confirming that calpain proteolytic activity occurs following Vacor treatment (Fig. 6, *E* and *F*). Since the processing is specific to proteins found in dendrites, calpains appear to only be activated downstream of SARM1 in dendrites and not in axons where an alternative degeneration pathway may exist downstream of SARM1 (see model in Fig. 7).

Discussion

SARM1 has been studied primarily in axons since its identification as a critical mediator of Wallerian degeneration (1, 28, 29). In this study, we sought to understand the localization and function of SARM1 in CNS neurons with more complex cellular morphology. We demonstrated that SARM1 is expressed throughout the neuron and can contribute not only to axon degeneration but also to programmed degeneration of

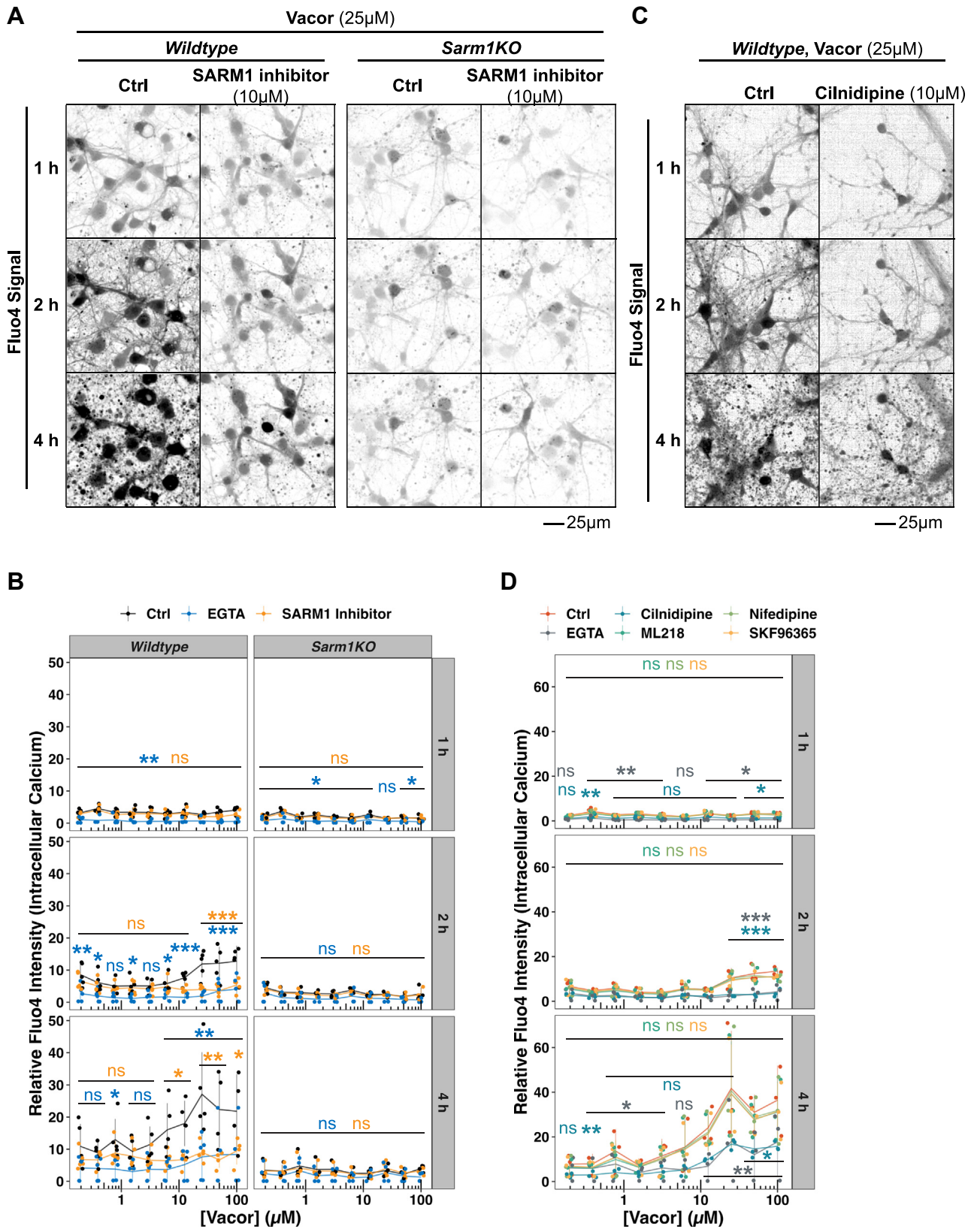

Figure 5. SARM1 activation increases intracellular calcium. *A*, representative images of Fluo4 intensity (intracellular calcium) in *wildtype* or *Sarm1KO* neurons treated with 25 μM of Vacor at 1, 2, and 4 h with or without SARM1 inhibitor (10 μM). *B*, quantification of relative Fluo4 intensity at 1, 2, and 4 h following treatment with increasing concentrations of Vacor with or without SARM1 inhibitor (10 μM) or EGTA (3 mM, Fig. S7*A* for EGTA images). *C*, representative images of Fluo4 intensity in *wildtype* neurons with or without cilnidipine (10 μM). *D*, quantification of relative Fluo4 intensity at 1, 2, and 4 h following treatment with increasing concentrations of Vacor with or without the indicated calcium channel blockers (Fig. S7*B* for other representative images). Statistical significance of effects by inhibitors was determined by two-way ANOVA using inhibitor treatment (including calpain inhibitor III, EGTA, SARM1 inhibitor, or cilnidipine treatment and others) and Vacor doses as two independent variables. When the effect of the inhibitor treatment was

the dendrite and the cell body in response to direct activation. Recently identified SARM1 agonists, CZ-48 and Vacor/Vacor mononucleotide (20, 23) allowed us to directly activate SARM1 in the absence of other injury or stress and more specifically dissect SARM1-dependent downstream signaling events in distinct subcellular compartments. Treatment of hippocampal neurons with these compounds resulted in SARM1-dependent degeneration of axons, dendrites, and cell bodies (Fig. 2). Surprisingly, SARM1 degeneration in the axons of hippocampal neurons was calpain independent, while degeneration of dendrites required Ca^{2+} influx and calpain activity. Taken together, these observations demonstrate that activation of SARM1 is sufficient to cause destruction of the entire CNS neuron, though the pathways that mediate degeneration downstream of SARM1 are distinct in axons and dendrites.

Previous studies have implicated calpain proteases in the degeneration of DRG axons following lesion or nerve growth factor withdrawal, where calpain inhibition robustly prevents axon degeneration (37, 41, 51). In our primary hippocampal neuron models, we also observed a requirement for calpain activity, but this was specific to dendrites and did not impact axon degeneration (Fig. 3, *A* and *B*). Our data show that a canonical axon-specific calpain substrate Nf-L is not processed following SARM1 activation, unlike the well-processed substrates found in both axons and dendrites (Fig. 6). This observation suggests that calpains are not activated in the axonal compartment downstream of SARM1 as is observed in DRG neurons. It is therefore possible that SARM1's downstream pathways may depend on neuron subtype and the expression or localization of specific factors. Indeed, our examination of specific calpains revealed that the dendrite-enriched calpain2 is the primary driver of degeneration in this cellular compartment. In contrast, the observation that hippocampal axons still degenerate in the absence of calpain activity suggests that distinct pathways drive this process. This dendrite selective role for calpains is distinct from what has been previously observed in sensory neurons and suggests that expression of calpains and other downstream effectors may result in a differential impact of SARM1 activation across neuronal subtypes.

Calpain inhibitor III and calpeptin, but not other calpain inhibitors including (2S,3S)-*trans*-Epoxysuccinyl-L-leucylamido-3-methylbutane ethyl ester, PD150606, and leupeptin, robustly protected dendrites from SARM1-dependent degeneration (Fig. S3). Potency, selectivity, and/or inhibition mechanism could underlie the difference. Although it is challenging to compare Ki and/or IC_{50} values across studies that used different assays, the two effective calpain inhibitors are reported to be most potent against calpain1 and 2 with reported Ki/IC_{50} of 50 nM or lower, compared to those that showed no protection whose Ki/IC_{50} are higher than 200 nM (43). Indeed, calpain2 knockdown partially protected dendrites from SARM1-induced degeneration (Fig. 3, *C*–*F*), suggesting that the potency against calpain2 is the primary driver of efficacy of calpain inhibitors in our study.

Our finding that calcium influx in dendrites *via* Cav2.2 channel can be regulated by SARM1 activity provides new insight into the pathways downstream of this NADase that drive degeneration. The impact of calcium influx has been extensively studied in models of axonal lesion, where diverse models such as mouse DRG/SCGs, zebrafish, and flies have revealed two distinct phases of calcium influx in Wallerian degeneration (39, 40, 42, 55–57). The first phase is transient and proximal to the axon injury site, while the second is a more widespread terminal phase of calcium influx that shortly precedes degeneration. There is evidence that the WLDS mutant protein (39) or SARM1 deletion (40, 42) can prevent the second phase of calcium influx, but their impact on the first phase remains to be resolved (39, 40, 55–57). We observed a SARM1-dependent calcium influx in response to Vacor activation that only occurred after two hours and was more pronounced at four hours after SARM1 activation (Fig. 5). This indicates that SARM1 activity does not contribute to an early influx of calcium in this experimental setup and supports the earlier findings that SARM1 deletion can specifically impact late-phase calcium influx. In Wallerian degeneration of DRG or SCG neurons, various calcium channels have been implicated in this calcium influx (40, 58, 59), where our data indicate that in primary hippocampal neurons the SARM1-dependent calcium influx is mediated by Cav2.2 as cilnidipine, but not nifedipine, blunted SARM1-dependent calcium influx (Figs. 5 and S7*B*). Although the specific mechanisms by which SARM1 regulates Cav2.2 activity remains unclear, it is possibly mediated directly by cADPR generated by SARM1 (20, 60, 61), or indirectly by NAD^+ loss. cADPR is involved in mobilizing downstream calcium fluxes as this metabolite has many roles in TIR/cADPR/calcium signaling defined in other pathways (62–64).

In this study, we defined a degenerative role for SARM1 in hippocampal neurons that is localization dependent, with calpains playing a critical role only in dendrites (Fig. 7). A key question remains regarding what pathway(s) execute axon degeneration downstream of SARM1 in hippocampal neurons. Our observation that SARM1-dependent axon degeneration in hippocampal neurons is independent of both calpain and caspase proteases indicates that it is driven by distinct pathways that have yet to be defined. In addition, this result suggests that the contribution of calpains to degeneration of specific cellular processes is not uniformly conserved across neuronal subtypes, and the previously observed role in DRG/SCGs may be specific to these sensory neurons given their unique morphology characterized by a single bifurcating axon. It will also be important to understand the contribution of SARM1 to degeneration of CNS neurons *in vivo* following the complex cellular insults that occur in neurodegenerative disease or following acute injury. Further studies will be needed

significant ($p < 0.05$), either (*B*) Tukey's or (*D*) Dunnett's post hoc test was performed and *p* values that are less than 0.05 for the effect of inhibitor treatment at the specific Vacor doses are shown in a color-matched manner in figure panels. Number of biologically independent experiments (n) are (*B*) four and (*D*) three. Data are represented as the mean ± standard deviation by *vertical lines* with individual data points shown by *small circles*. *$p < 0.05$, **$p < 0.01$, ***$p < 0.001$, ns $p \geq 0.05$. SARM1, sterile alpha and toll/interleukin receptor motif-containing 1.

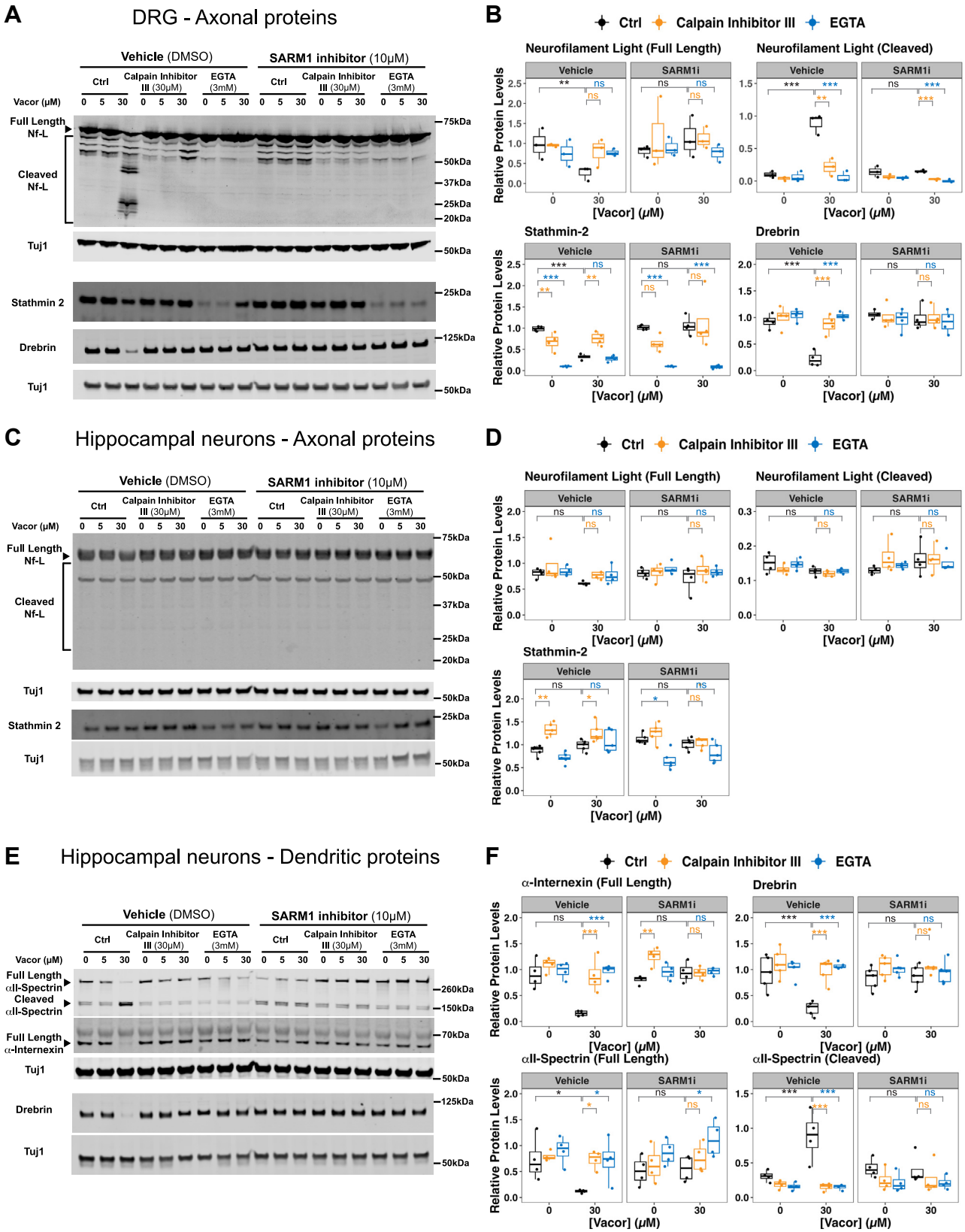

Figure 6. Calpains are downstream executors of SARM1 degeneration in dendrites, but not axons. Analysis of calpain substrate proteins that are known to be enriched in axons or dendrites in (*A* and *B*) mouse DRG neurons and (*C*–*F*) mouse hippocampal neurons treated with increasing concentrations of Vacor for 3 h with or without SARM1 inhibitor (10 μM), calpain inhibitor III (30 μM), and/or EGTA (3 mM). *A*, *C*, and *E* representative western blot images and (*B*, *D*, and *F*) quantification of relative levels are shown. *A* and *B*, levels of full-length and cleaved neurofilament light (Nf-L), stathmin2, and drebrin in mouse DRG neurons. *C* and *D*, levels of calpain substrates that are enriched in axons of cultured mouse hippocampal neurons. Full-length and cleaved neurofilament light (Nf-L) and stathmin 2. *E* and *F*, levels of calpain substrates that are enriched in dendrites of cultured mouse hippocampal neurons. Full-

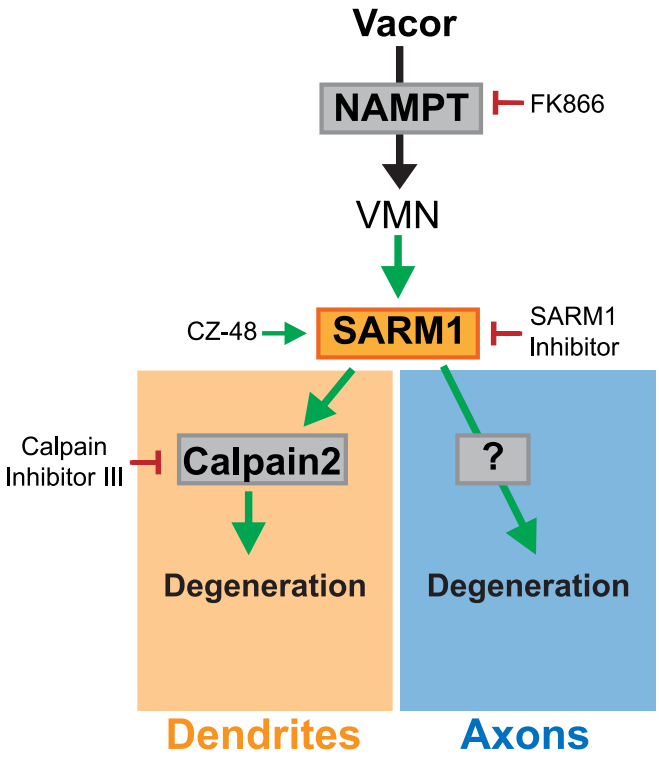

Figure 7. A model showing distinct degenerative pathways in different neuronal compartments in cultured mouse hippocampal neurons.

to fully understand the impact of SARM1 activity and downstream pathway interactions in axons, dendrites, and cell bodies of CNS neurons following diverse insults.

Experimental procedures

Table S1 lists all antibodies and Table S2 lists key reagents use in the Supporting Information.

Primary hippocampal neurons

Hippocampi were dissected from E16-E18 embryos of C57BL/6, CD-1 (Charles River Laboratories), or Sarm1-deficient mice (B6. 129X1-*Sarm1*^{tm1Aidi}/J, 018069, The Jackson Laboratory) in ice-cold Hibernate E solution. Dissected hippocampi were digested with ∼0.1 unit/hippocampus of papain in 1× PBS at 37 °C for 10 min and then incubated with DNAseI (3000 unit/ml) and heat inactivated-fetal bovine serum (HI-FBS) (half the volume of papain solution) at room temperature (RT) for 5 min. Hippocampi were dissociated by gentle pipetting (∼20 strokes) in the complete NbActiv4 medium (50 µl medium per hippocampus). The complete NbActiv4 medium consists of NbActiv4 (500 ml) supplemented with penicillin-streptomycin (5 ml, the final concentration at 100U/ml), glutamax (5 ml), and 5-floro-2-deoxyuridine (final concentration 1 µM). Dissociated hippocampi were spun down at 500rcf at 4 °C for 3 min, and the pellet was dissociated in the complete NbActiv4. Live cells were counted using a Cellometer Auto 2000 Cell Viability Counter (Nexcelom Bioscience), and the cells were plated on poly-D-lysine (PDL)-coated 96-well or 384-well plates at the density of 25,000 or 12,500 cells/well in 100 µl or 50 µl of the complete NbActiv4. Hippocampal neurons were grown for 8 to 12 days with half-medium changes every 7 days. Embryonic dates and neuronal culture duration (days *in vitro* (DIV)) within this range did not impact SARM1-dependent degeneration of neuronal compartments (Fig. S9). In Figures 3, *C–F* and S6, neurons were transduced with lentivirus on the day of plating (DIV0) at the concentration of 1 multiplicity of infection/cell and were used for experiments at DIV12. Primary hippocampal neurons from *wildtype* or *Sarm1*-deficient mice are hereafter referred to as *wildtype* or *Sarm1KO* neurons.

Primary DRG neuron

DRG were dissected from E12-E14 embryos of CD-1 (Charles River Laboratories) in ice-cold L15 medium. Dissected DRG were trypsinized by resuspending them in Trypsin-EDTA solution with shaking at 300 rpm at 37 °C for 15 min. After trypsinization, DRG were spun down at 1500rcf at RT for 2 min, rinsed once with L15 with 10% HI-FBS, dissociated in L15 with 10% HI-FBS, and triturated by slow pipetting (∼20 strokes). Triturated DRG neurons were spun down at 2000rcf at RT for 2 min and resuspended in 1 ml of the complete DRG medium. The complete DRG medium consists of neurobasal medium (500 ml) supplemented with B27 supplement (10 ml), 1M glucose (20 ml), glutamax (5 ml), penicillin-streptomycin (10 ml, the final concentration: 200U/ml), nerve growth factor (the final concentration at 25 ng/ml), and 5-floro-2-deoxyuridine (the final concentration at 1 µM). The number of viable cells were counted using Cellometer Auto 2000 Cell Viability Counter (Nexcelom Bioscience). DRG neurons were spun down again at 2000rcf for 2 min at RT. Pellet of DRG neurons were resuspended in the appropriate volume of the complete DRG medium so that the concentration of viable cells is 100000/µl. A total of 1.5 µl of dissociated DRG neurons were spotted in the middle of wells on 96w plates that are PDL- and laminin-coated. Plates were kept in the tissue-culture incubator (37 °C with 5% CO_2 and 95% humidity) for 10 min, and then the complete DRG medium was slowly added to each well (50 µl/well).

Immunocytochemistry

Primary hippocampal neurons were treated with CZ-48, Vacor, and/or other pharmacological tools in the complete NbActiv4 medium at 37 °C and 5% CO_2 for 8-16h. After

length α-internexin, full-length, and cleaved αII-spectrin, and drebrin under the same conditions as (*C* and *D*). Statistical significance of effects by Vacor and inhibitors were determined by two-way ANOVA using inhibitor and Vacor treatment as two independent variables. When the effect of the inhibitor treatment was significant ($p < 0.05$), Tukey's post hoc test was performed and *p* values that are less than 0.05 for the effect of Vacor treatment under the Ctrl (no pharmacological treatment) condition and of pharmacological treatment compared to the control group at the specific Vacor doses are shown in a color-matched manner in figure panels. Number of biologically independent experiments (n) are (*B*) 3 to 4, and (*D*, and *F*) 4 to 5. Data are presented by *boxplots* with individual data points shown by *small circles*. *$p < 0.05$, **$p < 0.01$, ***$p < 0.001$, ns $p \geq 0.05$. DRG, dorsal root ganglia; SARM1, sterile alpha and toll/interleukin receptor motif-containing 1.

treatment, neurons were fixed with 4% paraformaldehyde with 4% sucrose (Sigma-Aldrich, S0389) in 1× PBS at RT for 15 min. Fixed neurons were washed with 1× PBS once and then blocked in the blocking buffer at RT for at least 1h. The blocking buffer consists of 5% bovine serum albumin, 0.5% Triton X100 in 1× PBS. After blocking, neurons were incubated with primary antibodies diluted in the blocking buffer at 4 °C for at least 16 h. Neurons were then washed 3 times with 1× PBS, incubated with secondary antibodies diluted in the blocking buffer at RT for 1 h, and then washed again 3 times with 1× PBS.

Super resolution confocal imaging and quantification of axonal and dendritic localization

Neurons were plated on PDL-coated 96-well plate (Greiner Bio-One, 655946) for super resolution confocal imaging. Immunocytochemistry was done essentially in the same way as described above, except for fixation. For super resolution confocal imaging, cells were fixed with 4% paraformaldehyde with 4% sucrose in 1× PBS at RT for 10 min and then 100% MeOH at 4 ℃ for an additional 5 min for mitochondrial staining. Immunostained cells were imaged with a laser scanning confocal microscope (Leica SP8; Leica Microsystems, Inc), acquired with a 63×/1.4 numerical aperture (NA) oil objective in LIGHTNING super-resolution mode with a pixel size of 40 nm. Images were then processed using an adaptive processing algorithm. The representative images were generated by three-dimensional reconstruction using Imaris (Bitplane; https://imaris.oxinst.com/). To obtain accurate mitochondrial 3D structures, we used surface rendering and fluorescence thresholding. Quantification of axonal and dendritic localization was performed using ImageJ2 (National Institutes of Health; https://imagej.net/software/imagej2/), by profiling the fluorescence intensity of each channel by Plot_-Multicolor4.3 (65).

Liquid handling (plating, feeding, fixing, and immunostaining neurons on 384-well plates)

Neurons were resuspended in the complete NbActiv4 media at a density of 250,000 cells/ml. A Dynamic Devices Lynx liquid handler in a sterile cabinet was used to plate cells (12,500 cells/well in 50 µl media) into PDL-coated 384-well clear-bottom optical plates, with gentle resuspension of cells in the source reservoir prior to transfer to promote even plating density. Cell feeding was performed in the Lynx by removing 50% of the media and gently adding the complete media slowly to avoid cell disruption every 7 days. Immunostaining was performed as described in the "Immunocytochemistry" section, using a BioTek EL406 plate washer and Agilent Bravo liquid handler, integrated by HighRes Biosolutions, to gently transfer 1× PBS or reagents to neurons at each step.

Quantification of axon/dendrite degeneration and nuclear condensation

Immunostained neurons were imaged using the Opera Phenix High-Content Screening System (PerkinElmer) and images were quantified using the Harmony software (PerkinElmer; https://www.revvity.com/product/harmony-5-2-office-hh17000016). To acquire fluorescent images, we used built-in acquisition protocols for DAPI (excitation/emission at 375 nm/435–480 nm), Alexa488 (488 nm/500–550 nm), Alexa568 (561 nm/570–630 nm), and Alexa647 (640 nm/650–760 nm), and water-immersion 40× objective (NA = 1.1) using the confocal mode acquiring two z-slice images spaced 1 µm apart. Areas of axons or dendrites were quantified by applying the built-in spot analysis on images of respective channels. Total areas of axons or dendrites were quantified per well and per plate and normalized to the respective control values (*e.g.* mean of untreated *wildtype* wells) per plate. All the nuclei were detected by applying the built-in nucleus detection protocol on DAPI images and further classified into condensed or normal nuclei by applying a manual linear classifier that was trained using at least 50 nuclei per group.

Quantification of PAD6 signal

Cultured neurons were incubated with PC6 (50 µM) and CellMask deep red (Thermo Fisher Scientific C10046, 1:5000) for 2 h prior to imaging, in the complete NbActiv4 in the humidified incubator at 37 °C with 5% CO_2. One hour prior to imaging, SARM1 agonist and inhibitors were added by D300e digital dispenser (Tecan) and further incubated in the incubator. PAD6 signal was imaged using the Opera Phenix Plus High-Content Screening System (PerkinElmer) and images were quantified using the Harmony software (PerkinElmer). To acquire PAD6 and CellMask signal, we used built-in acquisition protocols for mTurquoise2-extended (excitation/emission at 405 nm/435–550 nm) and Alexa647 (640 nm/650–760 nm), respectively, and water immersion 63× (NA = 1.15) under the confocal mode acquiring two z-slice images spaced 0.5 µm apart, at 37 °C and with 5% CO_2. PAD6-positive area was quantified first by applying an intensity threshold for mTurquoise2-extended channel to select pixels with PAD6 signal above the background, and then by measuring the total numbers of pixels per well. The PAD6-positive area was normalized to the respective control values (mean of untreated *wildtype* wells) per plate. This way, we separated SARM1-specific activity that induced the widespread PAD6 signal throughout the cytoplasm from the background punctate signal that is likely caused by protonation of PC6 in the lysosomes and thus is independent of SARM1 activity.

Calcium imaging using Fluo4

Wildtype or *Sarm1KO* neurons were incubated with Fluo4 (1 µM) for 30 min prior to the compound addition, in the complete NbActiv4 in the humidified incubator at 37 °C with 5% CO_2. SARM1 agonist and inhibitors were added by D300e digital dispenser (Tecan) and imaging was started immediately. Fluo4 signal was imaged using the Opera Phenix Plus High-Content Screening System (PerkinElmer), and images were quantified using the Harmony software (PerkinElmer). To acquire Fluo4 signal, we used built-in acquisition protocol for Fluo4 (excitation/emission at 488 nm/500–550 nm) and water

immersion 20× (NA = 1.0) under the confocal mode at 37 °C with 5% CO_2. Fluo4 signal intensity was quantified first by applying the built-in spot analysis to define Fluo4-positive puncta. Secondly, corrected spot intensity of Fluo4 signal was integrated per each spot and then summarized per well at each time point. The summarized Fluo4 intensity was normalized to the mean intensity of the vehicle-treated well at the first time point (t = 0 min after addition of toxins and inhibitors) in each genotype per biological replicate.

Western blot

Equal numbers of cultured neurons underwent treatment, were lysed in equal volumes of lysis buffer (1× NuPAGE lithium dodecyl sulfate sample buffer and 1× NuPAGE Sample Reducing Agent), were denatured at 95 °C for 10 min, and were loaded per gel lane. Protein samples were electrophoresed on NuPAGE Novex 4 to 12% Bis-Tris Midi protein gels in 1× NuPAGE MOPS or MES SDS running buffer at 200V for 1 h at RT. Gels were transferred to nitrocellulose membranes with Tran-Blot Turbo Transfer System (Bio-Rad). Membranes were blocked with Odyssey blocking buffer (Li-Cor 927–40000) at RT for at least 1 h, incubated with primary antibodies overnight at 4 °C followed by 4× washes with TRIS-buffered saline with Tween at RT, and then incubated with secondary antibodies at RT for 1 h, followed by 4× washes with TRIS-buffered saline with Tween at RT. Li-Cor odyssey system was used for Western blot detection and quantification. The band intensities of proteins of interest were quantified using Image Studio Lite software (Li-Cor; https://www.licor.com/bio/image-studio-lite/) and normalized to those of loading control protein (*e.g.* Tuj1) per each lane. To quantify the calpain activity (Fig. 6), the signal intensities of full-length and cleaved substrates were separately quantified. Images of the full uncropped Western blot images can be found in the online Supporting Information.

NAD(H) quantification

Equal numbers of *wildtype* or *Sarm1KO* neurons plated on 96-well plates were treated with various concentrations of CZ-48, or Vacor for 16 h. Cellular NAD(H) levels were measured using NAD/NADH-Glo assay (Promega). Briefly, neuron plates were cooled to RT for 30 min, and the medium volumes were normalized to 50 µl per well. The NAD/NADH-Glo detection reagent was prepared while neuron plates were at RT and applied to neuron plates (50 µl/well). Plates were incubated at RT for 1 h with gentle horizontal shake at 300 rpm. Luminescence of each well was measured using EnVision Multimode Plate Reader (PerkinElmer).

mRNA quantification by real time quantitative PCR (RT-qPCR)

Total RNA was extracted from 50,000 neurons that were treated with DMEM (Ctrl) or transduced with lentivirus encoding shRNA against calpain1 or calpain2 (calpain1-shRNA or calpain2-shRNA) using RNeasy Plus micro kit (Qiagen), according to the manufacturer's instructions. Complementary DNA was generated from 60 ng of the total RNA using the SuperScript IV VILO Master Mix (Thermo Fisher Scientific), by incubating the reaction at 25 °C for 10 min, followed by 50 °C for 10 min and 85 °C for 5m. RT-qPCR was performed using Taqman Fast Advanced Master Mix (Thermo Fisher Scientific) with the following probes: calpain1 (Thermo Fisher Scientific Mm00482964), calpain2 (Thermo Fisher Scientific Mm00486669), and actin (Thermo Fisher Scientific, Mm02619580). The RT-qPCR reaction was performed with a QuantStudio 6 Flex system (Applied Biosystems) using the following thermal cycles: 50 °C for 15 min, 95 °C for 2 min, and then 40 cycles of 95 °C for 15 s, 60 °C for 1 min. The calpain1 and 2 mRNA levels were normalized to the actin mRNA levels within each sample. The actin-normalized calpain1 and 2 mRNA levels were then normalized to their levels in the control neurons (neurons that were treated with DMEM without lentivirus) per each biological replicate.

Synthesis of CZ-48, PC6, and SARM1 inhibitor

CZ-48 (66), PC6 (35), and SARM1 inhibitor 3-iodo-1H-pyrrolo[2,3-c]pyridine (36) were synthesized by following the methods described previously.

Mouse handling

All mouse procedures adhered to regulations and protocols approved by Denali Therapeutics Institutional Animal Care and Use Committee. Mice were housed under a 12-h light/dark cycle and had access to water and standard rodent diet *ad libitum*.

Experimental design, data collection, and statistical analysis

Each experiment consists of all the conditions that were directly compared, including genotype, variable doses of toxin treatment, and the presence of pharmacological treatment. Each condition consists of 1 to 3 technical replicates, such as wells in western blot and immunocytochemistry. Bulk of data were acquired and analyzed by automated systems in an unbiased manner. Super-resolution microscopy (Figs. 1*A*, S6, and S8) and western blot (Fig. 6) experiments were performed and analyzed in a nonblinded manner. Acquired data were averaged and/or normalized to the control condition (*e.g.* dimethyl sulfoxide-treated *wildtype* neurons) in each experiment. We then repeated experiments using biologically distinct samples, which indicate neurons prepared from different mice on a different day (typically one to several weeks apart). Averaged and/or normalized values from each biologically independent replicate was treated as independent unit (n), plotted, and reported in each Figure legend.

Statistical tests were performed by ANOVA using stats::aov function in R (Version 4.3.0; https://cran.r-project.org/) and independent variables were reported in Figure legend. An interaction effect between two independent variables was also assessed when running two-way ANOVA. When ANOVA indicated a significant ($p < 0.05$) effect of an independent variable of interest (*e.g.* genotype and pharmacological treatment), either Tukey's (if numbers of groups were three or less)

or Dunnett's (4 or more) post hoc test was further performed to compare specific points (e.g. the difference between two genotypes at a specific toxin dose) using pairs or contrast function from the emmeans R package (https://cran.r-project.org/web/packages/emmeans/index.html) (67). In Figure 3*D*, one-sample *t* test was performed using stats::t.test function in R, against the theoretical mean of 1 (mu = 1). *p* values that are less than 0.05 are reported in Figure panels using asterisks that represent the ranges of *p* values – ns, *, **, and *** indicate $p \geq 0.05$, $p < 0.05$, $p < 0.01$, and $p < 0.001$, respectively.

Data availability

The data described in the manuscript are contained within the manuscript as graphs. Raw data can be shared upon request—please contact the corresponding authors.

Supporting information—The article contains supporting information.

Acknowledgments—We thank Thomas Sandmann for statistical analysis support and manuscript feedback. We also thank members of Denali Therapeutics, especially Gil Di Paolo, for helpful discussions and comments on the manuscript. Funding for this work was provided by Denali Therapeutics, Inc.

Author contributions—T. M., C. K., J. C., J. C. D., J. D., and M. L., investigation; T. M., C. K., J. C. D., J. D., M. E. K. C., J. W. L., and L. A. K. methodology; T. M. and C. K., visualization; T. M., M. L., J. W. L., and L. A. K. conceptualization; T. M. and C. K., formal analysis; T. M. and L. A. K. project administration; T. M., C. K., J. W. L., and L. A. K. validation; T. M., J. W. L., and L. A. K. writing–original draft; T. M., C. K., J. C., J. C. D., J. D., A. L. B., A. P. T., M. L., M. E. K. C., B. M. F., J. W. L., and L. A. K. writing–review and editing; J. C. D. software; A. L. B., A. P. T., M. E. K. C., and B. M. F. resources; M. E. K. C., B. M. F., J. W. L., and L. A. K. supervision.

Conflict of interest—T. M., C. K., J. C., J. C. D., A. L. B., M. E. K. C., B. M. F., J. W. L., and L. A. K. are current employees and shareholders of Denali Therapeutics. J. D. G., A. P. T., and M. L. are former employees of Denali Therapeutics.

Abbreviations—The abbreviations used are: ADPR, adenosine diphosphate ribose; cADPR, cyclic-ADPR; CNS, central nervous system; DAPI, 4′,6-diamidino-2-phenylindole; DIV, days *in vitro*; DRG, dorsal root ganglion; HI-FBS, heat inactivated-fetal bovine serum; NA, numerical aperture; NMN, nicotinamide mononucleotide; NMNAT1, nicotinamide mononucleotide adenylyltransferase 1; PDL, poly-D-lysine; RT, room temperature; RT-qPCR, real time quantitative PCR; SARM1, sterile alpha and toll/interleukin receptor motif-containing 1; SCG, superior cervical ganglion; TIR, toll/interleukin receptor; WLDS, Wallerian degeneration slow.

References

1. Coleman, M. P., and Höke, A. (2020) Programmed axon degeneration: from mouse to mechanism to medicine. *Nat. Rev. Neurosci.* **21**, 183–196
2. Mcguinness, H. Y., Gu, W., Shi, Y., Kobe, B., and Ve, T. (2023) SARM1-Dependent axon degeneration : nucleotide signaling , neurodegenerative disorders, toxicity, and therapeutic opportunities. *Neuroscientist*. https://doi.org/10.1177/10738584231162508
3. Lunn, E. R., Perry, V. H., Brown, M. C., Rosen, H., and Gordon, S. (1989) Absence of Wallerian degeneration does not hinder regeneration in peripheral nerve. *Eur. J. Neurosci.* **1**, 27–33
4. Mack, T. G., Reiner, M., Beirowski, B., Mi, W., Emanuelli, M., Wagner, D., *et al.* (2001) Wallerian degeneration of injured axons and synapses is delayed by a Ube4b/Nmnat chimeric gene. *Nat. Neurosci.* **4**, 1199–1206
5. Araki, T., Sasaki, Y., and Milbrandt, J. (2004) Increased nuclear NAD biosynthesis and SIRT1 activation prevent axonal degeneration. *Science* **305**, 1010–1013
6. Conforti, L., Wilbrey, A., Morreale, G., Janeckova, L., Beirowski, B., Adalbert, R., *et al.* (2009) Wld S protein requires Nmnat activity and a short N-terminal sequence to protect axons in mice. *J. Cell Biol.* **184**, 491–500
7. Babetto, E., Beirowski, B., Janeckova, L., Brown, R., Gilley, J., Thomson, D., *et al.* (2010) Targeting NMNAT1 to axons and synapses transforms its neuroprotective potency *in vivo*. *J. Neurosci.* **30**, 13291–13304
8. Sasaki, Y., Vohra, B. P. S., Baloh, R. H., and Milbrandt, J. (2009) Transgenic mice expressing the Nmnat1 protein manifest robust delay in axonal degeneration *in vivo*. *J. Neurosci.* **29**, 6526–6534
9. Gilley, J., and Coleman, M. P. (2010) Endogenous Nmnat2 is an essential survival factor for maintenance of healthy axons. *Plos Biol.* **8**, e1000300
10. Osterloh, J. M., Yang, J., Rooney, T. M., Fox, A. N., Adalbert, R., Powell, E. H., *et al.* (2012) dSarm/Sarm1 is required for activation of an injury-induced axon death pathway. *Science* **337**, 481–484
11. Essuman, K., Summers, D. W., Sasaki, Y., Mao, X., Diantonio, A., and Milbrandt, J. (2017) The SARM1 Toll/Interleukin-1 receptor domain possesses intrinsic NAD^+ cleavage activity that promotes pathological axonal degeneration. *Neuron* **93**, 1334–1343.e5
12. Loring, H. S., Icso, J. D., Nemmara, V., and Thompson, P. R. (2020) Initial kinetic characterization of sterile alpha and toll/interleukin receptor motif-containing protein 1. *Biochemistry* **59**, 933–942
13. Horsefield, S., Burdett, H., Zhang, X., Manik, M. K., Shi, Y., Chen, J., *et al.* (2019) NAD+ cleavage activity by animal and plant TIR domains in cell death pathways. *Science* **365**, 793–799
14. Sporny, M., Guez-Haddad, J., Khazma, T., Yaron, A., Dessau, M., Shkolnisky, Y., *et al.* (2020) Structural basis for SARM1 inhibition and activation under energetic stress. *eLife* **9**, e62021
15. Di Stefano, M., Nascimento-Ferreira, I., Orsomando, G., Mori, V., Gilley, J., Brown, R., *et al.* (2015) A rise in NAD precursor nicotinamide mononucleotide (NMN) after injury promotes axon degeneration. *Cell Death Differ.* **22**, 731–742
16. Alexandris, A. S., Ryu, J., Rajbhandari, L., Harlan, R., McKenney, J., Wang, Y., *et al.* (2022) Protective effects of NAMPT or MAPK inhibitors and NaR on Wallerian degeneration of mammalian axons. *Neurobiol. Dis.* **171**, 105808
17. Sasaki, Y., Nakagawa, T., Mao, X., DiAntonio, A., and Milbrandt, J. (2016) NMNAT1 inhibits axon degeneration *via* blockade of SARM1-mediated NAD^+ depletion. *eLife* **5**, e19749
18. Figley, M. D., Gu, W., Nanson, J. D., Shi, Y., Sasaki, Y., Cunnea, K., *et al.* (2021) SARM1 is a metabolic sensor activated by an increased NMN/NAD+ ratio to trigger axon degeneration. *Neuron* **109**, 1118–1136.e11
19. Loreto, A., Hill, C. S., Hewitt, V. L., Orsomando, G., Angeletti, C., Gilley, J., *et al.* (2020) Mitochondrial impairment activates the Wallerian pathway through depletion of NMNAT2 leading to SARM1-dependent axon degeneration. *Neurobiol. Dis.* **134**, 104678
20. Zhao, Z. Y., Xie, X. J., Li, W. H., Liu, J., Chen, Z., Zhang, B., *et al.* (2019) A cell-permeant mimetic of NMN activates SARM1 to produce cyclic ADP-ribose and induce non-apoptotic cell death. *iScience* **15**, 452–466
21. Bratkowski, M., Xie, T., Thayer, D. A., Lad, S., Mathur, P., Yang, Y. S., *et al.* (2020) Structural and mechanistic regulation of the pro-degenerative NAD hydrolase SARM1. *Cell Rep.* https://doi.org/10.1016/j.celrep.2020.107999
22. Jiang, Y., Liu, T., Lee, C. H., Chang, Q., Yang, J., and Zhang, Z. (2020) The NAD^+-mediated self-inhibition mechanism of pro-neurodegenerative SARM1. *Nature* **588**, 658–663
23. Loreto, A., Angeletti, C., Gu, W., Osborne, A., Nieuwenhuis, B., Gilley, J., *et al.* (2021) Neurotoxin-mediated potent activation of the axon degeneration regulator SARM1. *eLife* **10**, e72823

24. Loreto, A., Antoniou, C., Merlini, E., Gilley, J., and Coleman, M. P. (2023) NMN: the NAD precursor at the intersection between axon degeneration and anti-ageing therapies. *Neurosci. Res.* https://doi.org/10.1016/j.neures.2023.01.004
25. Angeletti, C., Amici, A., Gilley, J., Loreto, A., Trapanotto, A. G., Antoniou, C., *et al.* (2022) SARM1 is a multi-functional NAD(P)ase with prominent base exchange activity, all regulated bymultiple physiologically relevant NAD metabolites. *iScience* **25**, 103812
26. Nan Hou, Y., Cai, Y., Hua Li, W., Ming He, W., Ying Zhao, Z., Jie Zhu, W., *et al.* (2022) A conformation-specific nanobody targeting the NMN-activated state of SARM1. *Nat. Commun.* **13**, 7898
27. Icso, J. D., and Thompson, P. R. (2022) The chemical biology of NAD+ regulation in axon degeneration. *Curr. Opin. Chem. Biol.* **69**, 102176
28. Krauss, R., Bosanac, T., Devraj, R., Engber, T., and Hughes, R. O. (2020) Axons matter: the promise of treating neurodegenerative disorders by targeting SARM1-mediated axonal degeneration. *Trends Pharmacol. Sci.* **41**, 281–293
29. Gerdts, J., Summers, D. W., Milbrandt, J., and DiAntonio, A. (2016) Axon self-destruction: new links among SARM1, MAPKs, and NAD+ metabolism. *Neuron* **89**, 449–460
30. Tao, J., and Rolls, M. M. (2011) Dendrites have a rapid program of injury-induced degeneration that is molecularly distinct from developmental pruning. *J. Neurosci.* **31**, 5398–5405
31. Ji, H., Sapar, M. L., Sarkar, A., Wang, B., and Han, C. (2022) Phagocytosis and self-destruction break down dendrites of Drosophila sensory neurons at distinct steps of Wallerian degeneration. *Proc. Natl. Acad. Sci. U. S. A.* **119**, e2204683119
32. Buonvicino, D., Mazzola, F., Zamporlini, F., Resta, F., Ranieri, G., Camaioni, E., *et al.* (2018) Identification of the nicotinamide salvage pathway as a new toxification route for antimetabolites. *Cell Chem. Biol.* **25**, 471–482.e7
33. LeWitt, P. (1980) The neurotoxicity of the rat poison vacor. A clinical study of 12 cases. *N. Engl. J. Med.* **302**, 73–77
34. Gallanosa, A. G., Spyker, D. A., and Curnow, R. T. (1981) Diabetes mellitus associated with autonomic and peripheral neuropathy after vacor rodenticide poisoning: a review. *Clin. Toxicol.* **18**, 441–449
35. Li, W. H., Huang, K., Cai, Y., Wang, Q. W., Zhu, W. J., Hou, Y. N., *et al.* (2021) Permeant fluorescent probes visualize the activation of SARM1 and uncover an anti-neurodegenerative drug candidate. *eLife* **10**, e67381
36. Hughes, R. O., Devraj, R., Bosanac, T., Jarjes-pike, R. A., Brearley, A. S., and Bentley, J. (2019) *Inhibitors of SARM1*. WIPO, WO2019236884A1
37. Yang, J., Weimer, R. M., Kallop, D., Olsen, O., Wu, Z., Renier, N., *et al.* (2013) Regulation of axon degeneration after injury and in development by the endogenous calpain inhibitor calpastatin. *Neuron* **80**, 1175–1189
38. Summers, D. W., DiAntonio, A., and Milbrandt, J. (2014) Mitochondrial dysfunction induces Sarm1-dependent cell death in sensory neurons. *J. Neurosci.* **34**, 9338–9350
39. Vargas, M. E., Yamagishi, Y., Tessier-Lavigne, M., and Sagasti, A. (2015) Live imaging of calcium dynamics during axon degeneration reveals two functionally distinct phases of calcium influx. *J. Neurosci.* **35**, 15026–15038
40. Loreto, A., Di Stefano, M., Gering, M., and Conforti, L. (2015) Wallerian degeneration Is executed by an NMN-SARM1-dependent late Ca2+ Influx but only modestly influenced by mitochondria. *Cell Rep.* **13**, 2539–2552
41. Cetinkaya-Fisgin, A., Luan, X., Reed, N., Jeong, Y. E., Oh, B. C., and Hoke, A. (2020) Cisplatin induced neurotoxicity is mediated by Sarm1 and calpain activation. *Sci. Rep.* **10**, 21889
42. Ko, K. W., Devault, L., Sasaki, Y., Milbrandt, J., and Diantonio, A. (2021) Live imaging reveals the cellular events downstream of sarm1 activation. *eLife* **10**, e71148
43. Ono, Y., Saido, T. C., and Sorimachi, H. (2016) Calpain research for drug discovery: challenges and potential. *Nat. Rev. Drug Discov.* **15**, 854–876
44. Ennes-Vidal, V., Menna-Barreto, R. F. S., Branquinha, M. H., Dos Santos, A. L. S., and D'Avila-Levy, C. M. (2017) Why calpain inhibitors are interesting leading compounds to search for new therapeutic options to treat leishmaniasis? *Parasitology* **144**, 117–123
45. Tsujinaka, T., Kajiwara, Y., Kambayashi, J., Sakon, M., Higuchi, N., Tanaka, T., *et al.* (1988) Synthesis of a new cell penetrating calpain inhibitor (calpeptin). *Biochem. Biophys. Res. Commun.* **153**, 1201–1208
46. Simon, D. J., Weimer, R. M., Mclaughlin, T., Kallop, D., Stanger, K., Yang, J., *et al.* (2012) A caspase cascade regulating developmental axon degeneration. *J. Neurosci.* **32**, 17540–17553
47. Gerdts, J., Summers, D. W., Sasaki, Y., DiAntonio, A., and Milbrandt, J. (2013) Sarm1-mediated axon degeneration requires both SAM and TIR interactions. *J. Neurosci.* **33**, 13569–13580
48. Shirao, T., Hanamura, K., Koganezawa, N., Ishizuka, Y., Yamazaki, H., and Sekino, Y. (2017) The role of drebrin in neurons. *J. Neurochem.* **141**, 819–834
49. Baudry, M., and Bi, X. (2016) Calpain-1 and calpain-2: the yin and yang of synaptic plasticity and neurodegeneration. *Trends Neurosci.* **39**, 235–245
50. Ozawa, Y., Hayashi, K., and Kobori, H. (2006) New generation calcium channel blockers in hypertensive treatment. *Curr. Hypertens. Rev.* **2**, 103–111
51. Ma, M., Ferguson, T. A., Schoch, K. M., Li, J., Qian, Y., Shofer, F. S., *et al.* (2013) Calpains mediate axonal cytoskeleton disintegration during Wallerian degeneration. *Neurobiol. Dis.* **56**, 34–46
52. Vega, I. E., Hamano, T., Propost, J. A., Grenningloh, G., and Yen, S. H. (2006) Taxol and tau overexpression induced calpain-dependent degradation of the microtubule-destabilizing protein SCG10. *Exp. Neurol.* **202**, 152–160
53. Cryns, V. L., Bergeron, L., Zhu, H., Li, H., and Yuan, J. (1996) Specific cleavage of α-fodrin during fas- and tumor necrosis factor- induced apoptosis is mediated by an interleukin-1β-converting enzyme/Ced-3 protease distinct from the poly(ADP-ribose) polymerase protease. *J. Biol. Chem.* **271**, 31277–31282
54. Benson, D. L., Mandell, J. W., Shaw, G., and Banker, G. (1996) Compartmentation of alpha-internexin and neurofilament triplet proteins in cultured hippocampal neurons. *J. Neurocytol.* **25**, 181–196
55. Tian, W., Czopka, T., and López-Schier, H. (2020) Systemic loss of Sarm1 protects Schwann cells from chemotoxicity by delaying axon degeneration. *Commun. Biol.* **3**, 49
56. Mishra, B., Carson, R., Hume, R. I., and Collins, C. A. (2013) Sodium and potassium currents influence wallerian degeneration of injured Drosophila axons. *J. Neurosci.* **33**, 18728–18739
57. Avery, M. A., Rooney, T. M., Pandya, J. D., Wishart, T. M., Gillingwater, T. H., Geddes, J. W., *et al.* (2012) Wld S prevents axon degeneration through increased mitochondrial flux and enhanced mitochondrial Ca^{2+} buffering. *Curr. Biol.* **22**, 596–600
58. Baccei, M. L., and Kocsis, J. D. (2000) Voltage-gated calcium currents in axotomized adult rat cutaneous afferent neurons. *J. Neurophysiol.* **83**, 2227–2238
59. Fuchs, A., Rigaud, M., Sarantopoulos, C. D., Filip, P., and Hogan, Q. H. (2007) Contribution of calcium channel subtypes to the intracellular calcium signal in sensory neurons: the effect of injury. *Anesthesiology* **107**, 117–127
60. Sasaki, Y., Engber, T. M., Hughes, R. O., Figley, M. D., Wu, T., Bosanac, T., *et al.* (2020) cADPR is a gene dosage-sensitive biomarker of SARM1 activity in healthy, compromised, and degenerating axons. *Exp. Neurol.* **329**, 113252
61. Li, Y., Pazyra-Murphy, M. F., Avizonis, D., Russo, M. T., Tang, S., Chen, C. Y., *et al.* (2022) Sarm1 activation produces cADPR to increase intra-axonal Ca++ and promote axon degeneration in PIPN. *J. Cell Biol.* https://doi.org/10.1083/jcb.202106080
62. Essuman, K., Milbrandt, J., Dangl, J. L., and Nishimura, M. T. (2022) Shared TIR enzymatic functions regulate cell death and immunity across the tree of life. *Science* **377**, eabo0001
63. Guse, A. H. (2015) Calcium mobilizing second messengers derived from NAD. *Biochim. Biophys. Acta Proteins Proteomics* **1854**, 1132–1137
64. Lee, H. C., and Zhao, Y. J. (2019) Resolving the topological enigma in Ca2+ signaling by cyclic ADP-ribose and NAADP. *J. Biol. Chem.* **294**, 19831–19843
65. Rueden, C. T., Schindelin, J., Hiner, M. C., DeZonia, B. E., Walter, A. E., Arena, E. T., *et al.* (2017) ImageJ2: ImageJ for the next generation of scientific image data. *BMC Bioinform.* **18**, 529
66. Chen, Z., Kwong, A. K. Y., Yang, Z., Zhang, L. L., Lee, H. C., and Zhang, L. L. (2011) Studies on the synthesis of nicotinamide nucleoside and nucleotide analogues and their inhibitions towards CD38 NADase. *Heterocycles* **83**, 2837–2850
67. Lenth, R. V. (2022) *emmeans: Estimated Marginal Means, aka Least-Squares Means*